

# Atomic Defects Profiling and Reliability of Amorphous Al<sub>2</sub>O<sub>3</sub> Metal–Insulator–Metal Stacks

P. La Torraca<sup>ID</sup>, F. Caruso<sup>ID</sup>, A. Padovani<sup>ID</sup>, Member, IEEE, G. Tallarida<sup>ID</sup>, S. Spiga<sup>ID</sup>, and L. Larcher<sup>ID</sup>

**Abstract**—We present a comprehensive characterization of amorphous alumina (a-Al<sub>2</sub>O<sub>3</sub>) high- $k$  dielectric in metal–insulator–metal (MIM) stacks, self-consistently extracting the space-energy distribution of a-Al<sub>2</sub>O<sub>3</sub> atomic defects and the related bond-breaking process parameters. Active defects are profiled via simultaneous simulation of current–voltage ( $I$ – $V$ ), capacitance–voltage ( $CV$ ), conductance–voltage (GV) (i.e., defect spectroscopy), and low-field  $I$ – $V$  hysteresis analysis. The defect energies extracted ( $E_{TH} = 1.55$  and  $3.55$  eV) are consistent with oxygen vacancies and aluminum interstitials. The voltage-dependent dielectric breakdown (VDDB) statistics of a-Al<sub>2</sub>O<sub>3</sub> is investigated using ramped voltage stress (RVS). The VDDB statistics show a complex and polarity-dependent breakdown statistics, correlating with defect distributions, which allows estimating the a-Al<sub>2</sub>O<sub>3</sub> bond-breaking parameters with the support of multiscale atomistic simulations of the breakdown process.

**Index Terms**—Amorphous alumina, atomic defects, breakdown, capacitance–voltage ( $CV$ ), high- $k$  dielectrics.

## I. INTRODUCTION

THE development of novel, emerging electron devices increasingly requires the adoption and combination of high dielectric constant (high- $k$ ) dielectrics [1], [2]. Among them, amorphous aluminum oxide (a-Al<sub>2</sub>O<sub>3</sub>) is a particularly interesting material, combining a high dielectric constant, a relatively large band gap, large band offsets with respect to silicon, high breakdown field, ease of fabrication with a low thermal budget, high uniformity, and excellent stability [3].

Manuscript received March 16, 2022; revised April 22, 2022; accepted April 28, 2022. Date of publication May 13, 2022; date of current version June 21, 2022. This work was supported in part by the H2020-EU ECSEL Project R3-PowerUP—300 mm Pilot Line for Smart Power and Power Discrete under Grant 737417. The review of this article was arranged by Editor J. Franco. (Corresponding author: P. La Torraca.)

P. La Torraca is with the Department of Sciences and Methods for Engineering, University of Modena and Reggio Emilia, 42122 Reggio Emilia, Italy (e-mail: paolo.latorraca@unimore.it).

F. Caruso is with CNR-Institute for Microelectronics and Microsystems (CNR-IMM), Unit of Agrate Brianza, 20864 Agrate Brianza, Italy, and also with the Dipartimento di Scienza dei Materiali, Università degli Studi di Milano-Bicocca, 20125 Milan, Italy.

A. Padovani and L. Larcher are with Applied Materials–MDLx Italy Research and Development, 42122 Reggio Emilia, Italy.

G. Tallarida and S. Spiga are with the CNR-Institute for Microelectronics and Microsystems (CNR-IMM), Unit of Agrate Brianza, 20864 Agrate Brianza, Italy (e-mail: sabina.spiga@mdm.imm.cnr.it).

Color versions of one or more figures in this article are available at <https://doi.org/10.1109/TED.2022.3172928>.

Digital Object Identifier 10.1109/TED.2022.3172928

Thanks to its electron-blocking capabilities, a-Al<sub>2</sub>O<sub>3</sub> found application in many conventional electronic components, such as CMOS transistors [3], high-electron-mobility transistors (HEMTs) [4], dynamic random access memories (DRAMs) [5], and radio frequency capacitors [6]. The same characteristics are currently been exploited in novel devices, such as charge-trapping memories [7], resistive random access memories (RRAMs) [8], ferroelectric tunnel junction (FTJ) memories [9], [10], magnetic tunnel junctions (MTJs) [11], [12] for spintronic applications, and Josephson junctions (JJJs) [13], [14] for solid-state quantum computing. The a-Al<sub>2</sub>O<sub>3</sub> also offers some degree of control on its atomic defects, allowing for its application as active resistance switching material in RRAMs [15], [16]. Other noticeable applications are the passivation of solar cells [17], [18] and the thermal environment design for phase-change memories (PCMs), thanks to its high thermal conductivity [19], [20].

Despite the wide application of a-Al<sub>2</sub>O<sub>3</sub>, the origin and properties of its atomic defects are still debated [21]–[23]. Moreover, the space-energy distribution of defects in the dielectric layers is well-known to play a key role in the device's reliability (e.g., breakdown, bias temperature instabilities, random telegraph noise) and performance (e.g., leakage current in 3D-NAND applications [24], nonlinear characteristics in DRAMs [25], nonuniform tunnel barrier in JJs [26]). The characterization of a-Al<sub>2</sub>O<sub>3</sub> properties and its precise defect profiling are thus of paramount importance for electronics, spintronics, and quantum computing applications.

In this article, we present a comprehensive electrical characterization of a-Al<sub>2</sub>O<sub>3</sub> in metal–insulator–metal (MIM) stacks. TaN/a-Al<sub>2</sub>O<sub>3</sub>/TaN MIM stacks of different thickness (5, 10, and 22.5 nm) are fabricated and characterized by measuring the current–voltage ( $I$ – $V$ ), capacitance–voltage ( $CV$ ), and conductance–voltage (GV) curves, double-sweep  $I$ – $V$  curves, and the voltage-dependent dielectric breakdown (VDDB) statistics. The space-energy distribution of atomic defects in the a-Al<sub>2</sub>O<sub>3</sub> layer and the bond-breaking energy are self-consistently extracted from electrical characterization with the support of multiscale atomistic simulations.

## II. EXPERIMENT

### A. Device Fabrication

TaN/a-Al<sub>2</sub>O<sub>3</sub>/TaN MIM capacitors are fabricated on highly doped n-type silicon wafers (resistivity  $\approx 1\text{--}3 \cdot 10^{-3} \Omega \cdot \text{cm}$ ).

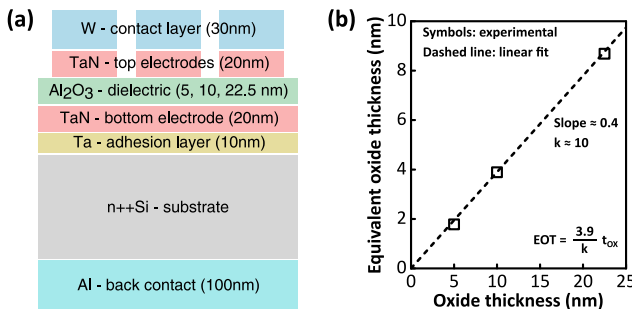


**Fig. 1.** (a) Schematic cross-sectional representation and (b) equivalent oxide thickness (EOT) of the fabricated MIM capacitors. EOT of different stacks is estimated from CV measurements at 10 kHz, 0 V. The resulting a-Al<sub>2</sub>O<sub>3</sub> permittivity is  $k \approx 10$ .

The native SiO<sub>2</sub> layer is removed by HF solution (5%) dipping for 3 min. A 10-nm-thick layer of Ta and 20 nm of TaN are deposited by RF sputtering (PVD75, Kurt J. Lesker Company<sup>1</sup>) at room temperature as the adhesion layer and bottom electrode, respectively (at a deposition pressure of  $3 \cdot 10^{-3}$  mbar). The 5-, 10-, and 22.5-nm Al<sub>2</sub>O<sub>3</sub> dielectric layers are deposited by atomic layer deposition (ALD) at 300 °C in a Savannah reactor (Cambridge Nanotech) using trimethylaluminum and water. Subsequently, 20-nm TaN top electrode and 30-nm W contact layer are deposited at room temperature by RF and dc sputtering, respectively, and patterned by optical lithography and lift-off process. The capacitor top electrodes' geometries are squares and circles with surface area ( $A$ ) ranging from  $1 \cdot 10^{-4}$  to  $16 \cdot 10^{-4}$  cm<sup>2</sup>. On the back side of the wafer, 100-nm Al is deposited by thermal evaporation to improve the back contact. Finally, the MIM stacks are subjected to a post-deposition thermal treatment in N<sub>2</sub> ambient at 300 °C for 20 min. Since the crystallization of ALD Al<sub>2</sub>O<sub>3</sub> occurs after high-temperature annealing above 800 °C–900 °C, the resulting Al<sub>2</sub>O<sub>3</sub> layers are still amorphous [27], [28]. Fig. 1(a) shows a schematic cross section of the resulting device. The thicknesses of a-Al<sub>2</sub>O<sub>3</sub> layers are measured by spectroscopic ellipsometry.

### B. Measurement

All the electrical measurements are carried out in air and dark ambient. Voltage bias is applied to the top electrode and the bottom electrode is held at ground.

The CV and GV characteristics are acquired at room temperature and at various frequencies from 220 Hz to 1 MHz using an Agilent E4980A precision LCR meter. Capacitance measurements at 10 kHz, 0 V are used to estimate a-Al<sub>2</sub>O<sub>3</sub> equivalent oxide thickness (EOT) ( $EOT = \epsilon_0 \cdot 3.9 \cdot A/C$ ) of different stacks [Fig. 1(b)]. From the slope of the linear fit of Fig. 1(b), a-Al<sub>2</sub>O<sub>3</sub> permittivity is estimated at  $k \approx 10$ , in accordance with previously reported values for ALD a-Al<sub>2</sub>O<sub>3</sub> (7–10 range) [29].

The room temperature  $I-V$  characteristics (Fig. 2) are measured by an HP4140B pA meter/dc voltage source. The voltage stimuli were double-sweep stepwise voltage ramps with a

0.05-V voltage step. The measurement delay time was set to 2 s, and the integration time was set to “Long,” resulting in a 4.56-s step length at low currents (below  $10^{-12}$  A), 3.28 s at medium currents ( $10^{-12} \text{ A} < I < 10^{-11}$  A), and 2.32 s at high currents (above  $10^{-11}$  A). Moreover, high-temperature  $I-V$  curves are measured at 90 °C, 150 °C, and 190 °C in air and in dark probe station equipped with hot chuck and by a Keysight B1500A semiconductor device analyzer using 16 PLC integration time, 0.05-V voltage step, and 2.32-s step length. All the  $I-V$  measurements are performed on 0.08-mm<sup>2</sup> area capacitors.

The VDDB distributions are extracted by RVS measurements performed by an HP4140B pA meter/dc voltage source. Four breakdown distributions are achieved for each dielectric thickness by considering two different voltage ramps (0.1 and 1 V/s) and for both negative and positive biases applied to the top electrode. During the voltage stress, the capacitor leakage current is monitored, and the breakdown voltage is recorded. More than 30 capacitors are measured to generate each distribution. These measurements are performed at room temperature on 0.04-mm<sup>2</sup> area capacitors.

### III. CHARACTERIZATION OF DEFECTS IN AMORPHOUS ALUMINA

The physical properties and space-energy distribution of the defects in the considered TaN/a-Al<sub>2</sub>O<sub>3</sub>/TaN MIM stacks are investigated with the support of GINESTRA<sup>2</sup> multiscale simulation software [30]. The charge transport through MIM stacks is modeled accounting for the different conduction mechanisms relevant in high- $k$  dielectrics, such as direct and Fowler–Nordheim tunneling, conduction/valence band carrier drift, and trap-assisted tunneling (TAT). Importantly for defects' profiling, the TAT is modeled according to the multi-phonon theory [31]–[33], accounting for electron–phonon coupling and atomic lattice relaxation associated with charge trapping. In the adopted framework, the charge transport phenomena, the stack electrostatics, the charge trapping/emission dynamics to/from defects in the dielectric, the charge occupancy in the defects, and the related temperature dependencies are self-consistently calculated.

Fig. 2 illustrates the experimental current density of the considered TaN/a-Al<sub>2</sub>O<sub>3</sub>/TaN MIM stacks. Interestingly, a low-field current hysteresis is observed in thicker stacks (i.e., 10- and 22.5-nm-thick a-Al<sub>2</sub>O<sub>3</sub> layer), while it is not detected for the 5-nm-thick a-Al<sub>2</sub>O<sub>3</sub> layer. Such behavior is typically overlooked, as the widely adopted single voltage sweep measurements only reveal half of the current hysteresis [34], [35], often erroneously associated with direct tunneling [35], [36]. The current hysteresis is instead due to the transient dynamics of charge trapping (emission) to (from) defects located near electrode interfaces and characterized by a thermal ionization energy ( $E_{TH}$ ) aligned with the stack Fermi level ( $E_F$ ) [37], [38]. During each RVS step, the trapping/emitting regions start at the electrodes' interfaces and progressively extend into the dielectric bulk. In the 10- and 22.5-nm a-Al<sub>2</sub>O<sub>3</sub> layers, the oxide is sufficiently thick to sustain such transient dynamics

<sup>1</sup>Registered trademark.

<sup>2</sup>Trademarked.

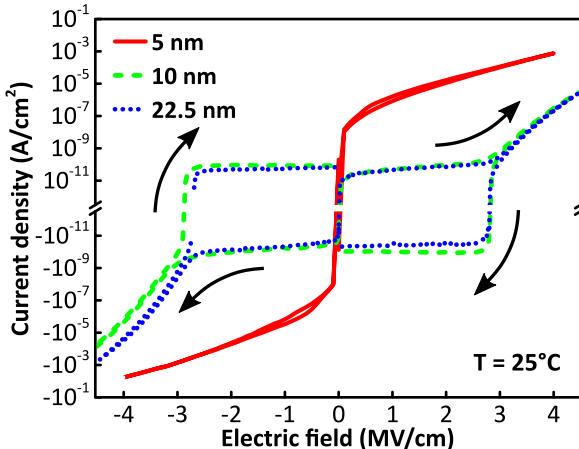


**Fig. 2.** Experimental results of the transient current density of TaN/a-Al<sub>2</sub>O<sub>3</sub>/TaN MIM stacks with different thickness (solid red line: 5 nm; dashed green line: 10 nm; dotted blue line: 22.5 nm). The curves are plotted in a log-plot with sign, highlighting the current hysteresis emerging in the low-field region ( $|E| < 3$  MV/cm) of the 10- and 22.5-nm stacks. Little variation is exhibited by the 5-nm stack. The black arrows show the hysteresis loops' directions.

for all the duration of the ramp step. In the 5-nm-thick a-Al<sub>2</sub>O<sub>3</sub> layer, this transient dynamic is rapidly settled, and a steady-state conduction within the ramp step length is reached. A small variation in the 5-nm stack current density is observed during the second part of the voltage double sweep, which can be ascribed to a charge trapping/detrapping mechanism or a defect generation process.

The 5-nm TaN/a-Al<sub>2</sub>O<sub>3</sub>/TaN stack, reaching a steady-state condition in the measurement voltage range, is characterized using a defect spectroscopy technique [39]–[41]. The defects are profiled using the GINESTRA defect spectroscopy tool [41], which allows extracting the defects' energy and spatial distributions from the interpretation of stack electrical measurements (i.e.,  $I$ - $V$ ,  $CV$ , and  $GV$  curves); see Fig. 3. The information provided by temperature dependence of the  $I$ - $V$  curve is used for estimating the defects' relaxation energy ( $E_{\text{REL}}$ ) [33]. In this work  $E_{\text{REL}}$  is considered constant among the defects, thus independent on the defects'  $E_{\text{TH}}$  distribution. This approach is a useful simplification that proved effective in previous works [25], [42], [43]. The extracted materials' parameters, reported in Table I, agree with the experimental [35], [38], [44] and *ab initio* [21], [45]–[47] results in the literature. The defects' properties agree with those of positively charged oxygen vacancies and aluminum interstitials. For sake of simplicity, in this work the defects are assumed to be oxygen vacancies, as they are reported as the more abundant and stable configuration for the considered material system [46]. Considering aluminum interstitials would just require accounting for a different initial charge state. This would affect the device electrostatics, possibly leading to some variation in further extracted parameters. The other defect parameters reported in Table I are the result of the following analysis. The extracted defect distribution [Fig. 3(a)] shows a defect density peaking at  $2 \cdot 10^{19} \text{ cm}^{-3}\text{eV}^{-1}$  in the a-Al<sub>2</sub>O<sub>3</sub> layer.  $E_{\text{TH}}$  is distributed between 1.5 and 3.3 eV. These defect parameters allow correctly simulating the experimental  $I$ - $V$  characteristics [Fig. 3(b)] along with the current temperature

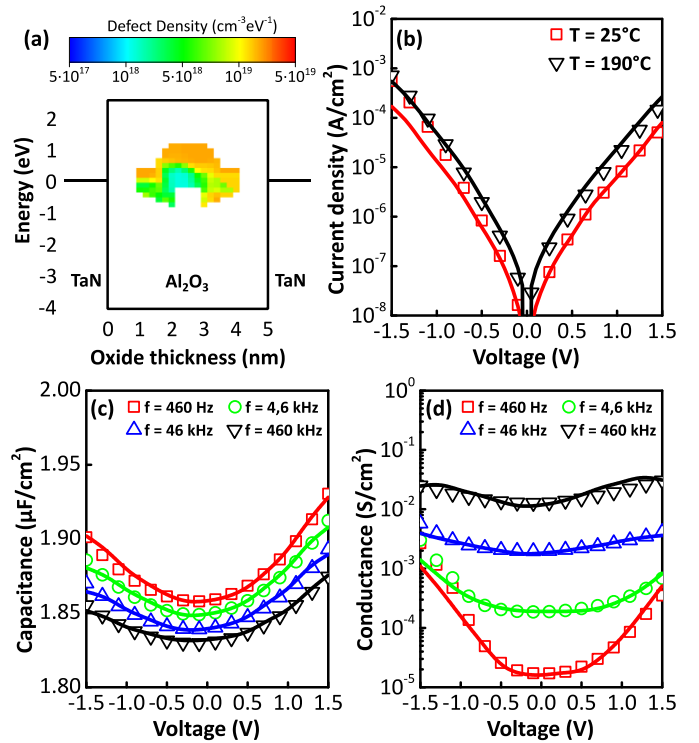


**Fig. 3.** Results of defect spectroscopy characterization of defects in a TaN-5-nm a-Al<sub>2</sub>O<sub>3</sub>/TaN stack. (a) Band diagram of the stack with the extracted defect energy spatial distribution, where colors represent defect density. (b) Experimental current densities' characteristics at various temperatures (symbols) and simulated curves using the extracted defect distribution (lines). Only the curves at 25 °C (red lines and squares) and 190 °C (black lines and squares) are shown. (c) Experimental  $CV$  curves at various frequencies (symbols) and corresponding simulated curves using the extracted defect distribution (lines). (d) Experimental  $GV$  curves at various frequencies (symbols) and simulated ones using the extracted defect distribution (lines).

dependence (for sake of clarity, only the curves at the two extreme temperatures are shown, i.e., 25 °C and 190 °C). The same defect distribution also allows reproducing the experimental  $CV$  [Fig. 3(c)] and  $GV$  [Fig. 3(d)] curves, measured at different frequencies. Interestingly, the asymmetry in the extracted defect distribution correlates with the experimental  $CV$  and  $GV$  characteristics, both exhibiting an asymmetric low-frequency behavior. The strong and simultaneous agreement between the experimental electrical measurements and the respective simulations demonstrates the consistency of the extracted defects' properties. Simulations allow extracting  $E_{\text{REL}} = 0.45$  eV, and the same value is used for the analysis of 10- and 22.5-nm-thick oxides.

Thicker TaN/a-Al<sub>2</sub>O<sub>3</sub>/TaN stacks (i.e., 10 and 22.5 nm) exhibit the effects of a transient dynamic at low field (i.e., the current hysteresis), and therefore the defect spectroscopy technique (which works on steady-state curves) can only be correctly applied at high field, thus limiting the characterization domain. The defects are thus characterized by interpreting the  $I$ - $V$  curve current hysteresis, which correlates with the defects' properties [38]. The hysteresis amplitude  $I_H$  at a specific ramp step is related to the RVS step amplitude  $V_{\text{STEP}}$  and step length  $t_{\text{STEP}}$ , and the density of defects available for

**TABLE I**  
MATERIALS AND DEFECT PARAMETERS

TaN				
WF	Work Function (eV)	4.55		
a-Al <sub>2</sub> O <sub>3</sub>				
BG	Band gap (eV)	6.4		
$\chi$	Electron affinity (eV)	2		
$m_T$	Electron tunneling effective mass	$0.5 m_0$		
k	Permittivity	10		
Defects in a-Al <sub>2</sub> O <sub>3</sub> (Oxygen Vacancy)				
Q	Empty state charge (e)	+1		
$\sigma$	Capture cross section (cm <sup>2</sup> )	$2 \cdot 10^{-14}$		
E <sub>PH</sub>	Phonon energy (eV)	0.05		
Extracted parameters				
	5nm	10nm	22.5nm	
E <sub>REL</sub>	Relaxation energy (eV)	0.45	0.45 <sup>b</sup>	0.45 <sup>b</sup>
E <sub>TH</sub>	Thermal ionization energy (eV)	1.5-3.3 <sup>a</sup>	1.55-3.55	1.55-3.55
DD <sub>TOP</sub>	Top distribution defect density (cm <sup>-3</sup> eV <sup>-1</sup> )	- <sup>a</sup>	$4.5 \cdot 10^{18}$	$9.5 \cdot 10^{18}$
DD <sub>BOT</sub>	Bottom distribution defect density (cm <sup>-3</sup> eV <sup>-1</sup> )	- <sup>a</sup>	$0.5 \cdot 10^{18}$	$0.5 \cdot 10^{18}$
t <sub>TOP</sub>	Top distribution thickness (nm)	- <sup>a</sup>	5	5
t <sub>BOT</sub>	Bottom distribution thickness (nm)	- <sup>a</sup>	5	17.5

<sup>a</sup>The 5 nm stack defect distribution is estimated via defect spectroscopy, resulting in the complex distribution shown in Fig. 3a.

<sup>b</sup>Extracted from 5 nm stack, used for the simulation of the 10nm and 22.5nm stacks.

charge trapping/emission DD<sub>TOT</sub>, as

$$I_H \propto V_{\text{STEP}} \cdot t_{\text{STEP}}^{-\alpha} \cdot \text{DD}_{\text{TOT}} \quad (1)$$

where  $\alpha$  is a fitting parameter, typically close to 1 [37], [48], [49]. The low-field current hysteresis indicates the presence of defects in the a-Al<sub>2</sub>O<sub>3</sub> layer, located near electrode interfaces at the cathode Fermi level  $E_F$  [37], [38], [49]. To account for constant low-field hysteresis amplitudes and asymmetry of the experimental high-field currents, in the simulations we considered two rectangular defect distributions near top and bottom electrodes, DD<sub>TOP</sub> and DD<sub>BOT</sub>, respectively. This results in DD<sub>TOT</sub> = DD<sub>TOP</sub> + DD<sub>BOT</sub>.

The low-field hysteresis also indicates a significant spread of the defect energy  $E_{\text{TH}} = 1.5-3$  eV [38]. This range agrees with  $E_{\text{TH}}$  spread extracted on the 5-nm stack via defect spectroscopy. The simulation of the transient current hysteresis amplitude allows extracting the total defect density  $\text{DD}_{\text{TOT}} \approx 5 \cdot 10^{18}$  and  $1 \cdot 10^{19}$  cm<sup>-3</sup>eV<sup>-1</sup> for the 10- and 22.5-nm stacks, respectively.

The defect distributions close to top and bottom electrodes, DD<sub>TOP</sub> and DD<sub>BOT</sub>, are extracted from the simulation of high-field regions of the  $I-V$  curve; see Table I. As shown in Fig. 4(c), the experimental results are accurately reproduced, both at low and high fields. The extracted defect distributions are asymmetric, with the defects concentrated within 5 nm from the top electrode, consistently with the asymmetry of the electrical curves. The extracted  $E_{\text{TH}}$  and their respective densities well compare with the values extracted from the defect spectroscopy of the 5-nm stack.

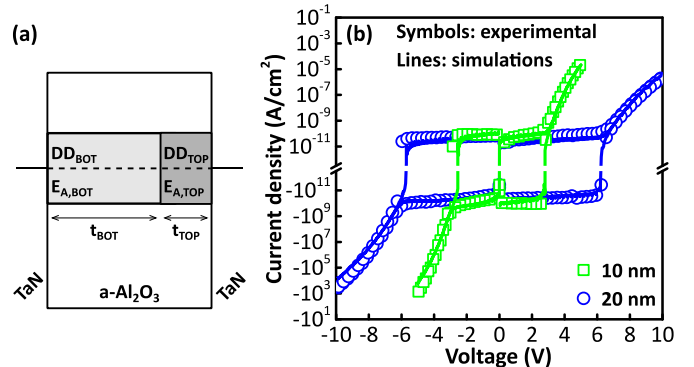


**Fig. 4.** Results of characterization of defects in thick a-Al<sub>2</sub>O<sub>3</sub> stacks by  $I-V$  hysteresis fitting. (a) Band diagram of TaN/a-Al<sub>2</sub>O<sub>3</sub>/TaN stacks considered for  $I-V$  and breakdown characterization. Both the stacks include two defect distributions with density DD<sub>TOP</sub> and DD<sub>BOT</sub> accounting for the defects near the top and bottom electrodes, respectively. Defect distributions are t<sub>TOP</sub> and t<sub>BOT</sub> thick, respectively, adjacent to the respective electrodes and aligned with the stack Fermi level. The zero-field activation energy of the defect generation process in the two regions is E<sub>A,TOP</sub> and E<sub>A,BOT</sub>, respectively. (b) Current densities of the 10- and 22.5-nm TaN/a-Al<sub>2</sub>O<sub>3</sub>/TaN stacks measured (symbols) and simulated using extracted defect distribution (lines).

To summarize, the electrical characteristic of the considered TaN/a-Al<sub>2</sub>O<sub>3</sub>/TaN stacks are explained by the presence of a defect band in the a-Al<sub>2</sub>O<sub>3</sub> layer with  $E_{\text{TH}}$  comprised between 1.55 and 3.55 eV. These energy levels are compatible with oxygen vacancies and aluminum interstitials, as calculated using *ab initio* calculations [46]. In the thin (5-nm) stack, the defect density is higher ( $2 \cdot 10^{19}$  cm<sup>-3</sup>eV<sup>-1</sup>). In thicker stacks (10 and 22.5 nm), the asymmetry is more pronounced, with most of the defects located in a 5-nm-thick region near the top electrode. The high defect density extracted in the thin stack could be ascribed to higher defect concentration at the electrode/dielectric interfaces, which is more important in thinner stacks [50]. The fabrication process might also lead to a higher defect density near the top electrode, which would affect both the thin and thick samples, such as sputtering damage [51], [52] and metallization-induced oxygen scavenging [53]. Finally, the differences found in thicker samples may be the result of the different growth times and thermal budgets. The origin of the reported differences in defectivity is currently being investigated.

#### IV. BREAKDOWN IN AMORPHOUS ALUMINA

The degradation and breakdown of the a-Al<sub>2</sub>O<sub>3</sub> layer in the considered MIM stacks are investigated using RSV to extract VDDB distribution [54], [55]. The experimental data are analyzed and interpreted in the framework of the thermochemical model of bond-breaking [56], [57] (also referred as the E-model [58]). Breakdown simulations are performed using GINESTRA multiscale simulation software [30].

Fig. 4 shows the VDDB distributions obtained from RSV performed using different voltage rates, both for positive [Fig. 5(a)-(c)] and negative [Fig. 5(d)-(f)] voltage ramps. All the VDDB distributions are consistent across different ramp rates (i.e., 0.1 and 1 Vs<sup>-1</sup>), preserving their shape and exhibiting a horizontal shift as expected

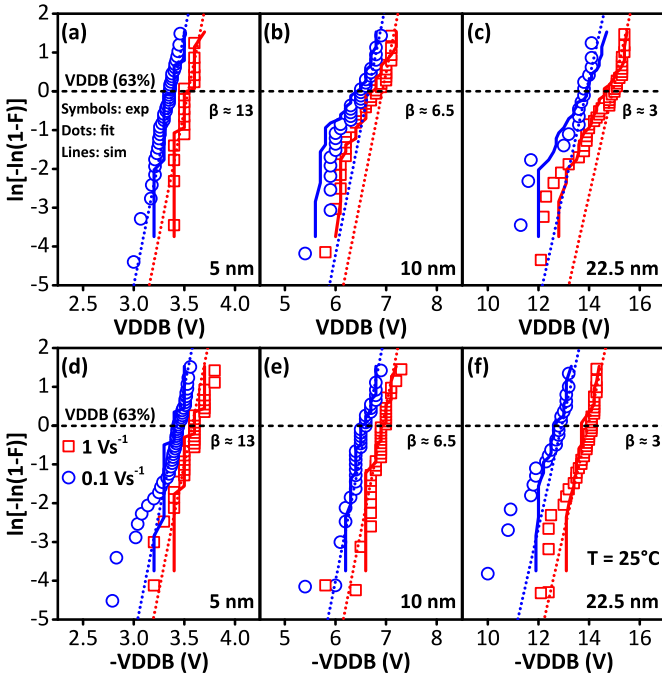


**Fig. 5.** Experimental (symbols) and simulated (solid lines) VDDB distributions measured on TaN/a-Al<sub>2</sub>O<sub>3</sub>/TaN stacks subjected to RVS with different polarities and at different ramp rates (red square: 1 Vs<sup>-1</sup>; blue circle: 0.1 Vs<sup>-1</sup>). Linear fits of distributions (dotted lines) obtained using the reported Weibull slope  $\beta$  are included for reference. (a) 5-nm, (b) 10-nm, and (c) 22.5-nm stacks under positive RVS. (d) 5-nm, (e) 10-nm, and (f) 22.5-nm stacks under negative RVS.

theoretically [54], [55]. The VDDB results are in excellent agreement with previously reports [35], [59], confirming the statistical relevance of the data. The extracted breakdown electric field ( $E_{BD} \approx 6 \text{ MVcm}^{-1}$ ) is consistent across different stack thicknesses, also in accordance with previously reported values [34], [35].

The VDDB distributions of the 5-nm stacks are symmetric with respect to the ramp polarity and follow a unimodal Weibull distribution with slope  $\beta \approx 13$  (shown in dot lines in Fig. 4). Conversely, thicker stacks (i.e., 10 and 22.5 nm) have an asymmetrical distribution, exhibiting a bimodal trend for positive voltage stresses. Negative VDDB distributions closely follow a unimodal Weibull distribution with  $\beta \approx 6.5$  and 3 for the 10- and 22.5-nm stacks, respectively. The same parameters allow fitting unimodal Weibull distributions to the highest quartile of the respective positive VDDB distributions. The inverse relationship between  $\beta$  and oxide thickness is consistent with RSV breakdown dynamics according to the thermochemical model [55].

This framework is used to estimate the atomistic parameter of the bond-breakage process, i.e., the bond dipole moment  $p_0$  and the zero-field activation energy  $E_A$ . The bond dipole moment  $p_0$  is estimated from VDDB distributions measured using different ramp rates [55]. In the presented analysis, the voltage difference between VDDB distributions is evaluated at the characteristic breakdown voltage  $V_{63}$ , corresponding to a failure rate of 63% (horizontal dashed line in Fig. 5). According to the thermochemical model of bond-breaking, in case of a constant stress voltage (CSV), the effective bond-breaking activation energy  $E_{A,\text{EFF}}$ , accounting for the

field induced stretching of the bonds, has been shown to be [60]

$$E_{A,\text{EFF}} = E_A - p_0 \left( \frac{2+k}{3} \right) E_{\text{TEST}} = k_B T \ln(G_0 \cdot t_{63}) \quad (2)$$

where  $k$  is the oxide permittivity,  $E_{\text{TEST}}$  is the constant electric field applied to the oxide,  $k_B$  is the Boltzmann's constant,  $T$  is the temperature,  $G_0$  is the bond vibration frequency, and  $t_{63}$  is the characteristic breakdown time (extracted from CSV time-dependent dielectric breakdown Weibull plots). From the equivalence between CVS tests and RVS tests reported in [55], an equivalent definition of  $E_{A,\text{EFF}}$  for RVS tests is obtained

$$E_{A,\text{EFF}} = E_A - p_0 \left( \frac{2+k}{3} \right) E_{63} = k_B T \ln(G_0 \cdot t_0) \quad (3)$$

where  $E_{63}$  is the characteristic breakdown electric field (extracted from VDDB Weibull plots, corresponding to  $V_{63}$ ), and  $t_0$  is a ramp-related parameter

$$t_0 = \frac{\Delta \tau}{1 - e^{-\gamma \frac{\Delta V}{t_{ox}}}} \quad (4)$$

where  $\gamma$  is the field acceleration factor,  $t_{ox}$  is the oxide thickness, and  $\Delta \tau$  and  $\Delta V$  are the RVS step time length and voltage height, respectively. Equating (3) for two different RVS with the same step voltage height  $\Delta V$  and different step time lengths  $\Delta \tau_1$  and  $\Delta \tau_2$  allows estimating  $p_0$  as

$$p_0 = \frac{k_B T}{\left(\frac{2+k}{3}\right)} \frac{t_{ox}}{(V_{63,2} - V_{63,1})} \ln\left(\frac{\Delta \tau_1}{\Delta \tau_2}\right) \quad (5)$$

where  $V_{63,1}$  and  $V_{63,2}$  are the characteristic breakdown voltages of the two ramps corresponding to  $\Delta \tau_1$  and  $\Delta \tau_2$ , respectively.

The estimated  $p_0$  values are shown in Fig. 6(a), ranging from  $p_0 \approx 3 \text{ e}\AA$  for the 5-nm stacks up to  $p_0 \approx 5.4 \text{ e}\AA$  for the 10-nm stacks, in excellent agreement with those reported in the literature (from 2.9 to 7  $\text{e}\AA$ ) [57]. Since alumina is amorphous, some degree of variation in the bond dipole moment is expected. For sake of simplicity,  $p_0 = 4 \text{ e}\AA$  is considered in the rest of the analysis to calculate  $E_A$ .

The effective activation energies  $E_{A,\text{EFF}}$  for different oxide thicknesses and stress polarities are calculated according to the right-hand side of (3) and plotted as a function of the characteristic breakdown electric field in Fig. 6(b). In this work,  $G_0 = 10^{14} \text{ Hz}$  is assumed. As the bond vibration frequency is typically in the  $10^{12}$ – $10^{14}$ -Hz range, this assumption could introduce a very small error in  $E_{A,\text{EFF}}$  estimate (<0.12 eV).

The zero-field activation energy  $E_A$  is then extracted from a linear fitting as the intercept  $E_{A,\text{EFF}}$  at zero field. The value extracted is consistent for all the three thicknesses ( $E_A \approx 1.9 \text{ eV}$ ) and does not depend on polarity. We verified that this value is negligibly affected by  $p_0$ : Fig. 6(b) includes error bars accounting for  $p_0$  variations shown in Fig. 6(a). All the experimental data match the slope of the linear fit ( $p_0 = 4 \text{ e}\AA$ ), validating the dipole moment estimate.

The VDDB distributions are simulated using GINESTRA, describing the bond-breaking process according to the thermochemical model [61]–[64] and accounting for the randomness of the process using the Monte-Carlo method.

An excellent agreement between the measurements and simulations is found considering the defects' properties previously

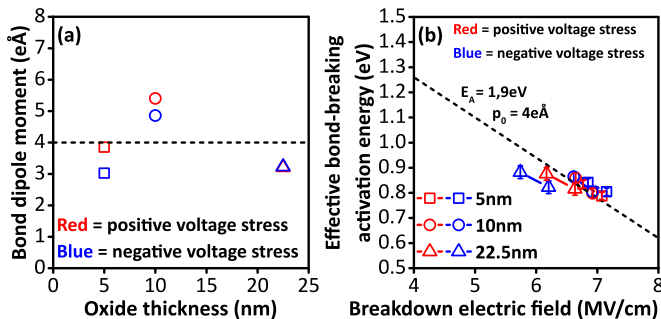


**Fig. 6.** (a) Bond dipole moment extracted from VDDB distributions at different ramp rates shown in Fig. 5. (b) Effective bond-breaking activation energy  $E_{A,\text{EFF}}$  versus characteristic breakdown electric field  $E_{63}$  as calculated from VDDB distributions of Fig. 5. Connected symbol pairs correspond to experiments at two different ramp rates. The included error bars show the uncertainty due to the bond dipole moment range extracted in Fig. 6(a). The line corresponding to  $p_0 = 4 \text{ eÅ}$  and  $E_A = 1.9 \text{ eV}$  is included (black dashed line).

**TABLE II**  
AMORPHOUS ALUMINA DEFECT GENERATION PARAMETERS

		5nm	10nm	22.5nm
$G_0$	Frequency prefactor (Hz)	$10^{14}$	$10^{14}$	$10^{14}$
$p_0$	Bond dipole moment (eÅ)	4	4	4
$E_{A,\text{TOP}}$	Top zero-field activation energy (eV)	$2.4 \pm 0.05$	$2.4 \pm 0.05$	$2.3 \pm 0.05$
$E_{A,\text{BOT}}$	Bottom zero-field activation energy (eV)	$2.4 \pm 0.05$	$2.35 \pm 0.1$	$2.35 \pm 0.1$

extracted (see Table I) and the thermochemical bond-breaking parameters reported in Table II. The simulations results are depicted in Fig. 5 as solid lines.

Interestingly, considering the estimated dipole moment  $p_0 = 4 \text{ eÅ}$ , the zero-field activation energy  $E_A$  extracted using GINESTRA is considerably higher ( $E_A \approx 2.4 \text{ eV}$ ) than the value extracted using the thermochemical model [57] (3).

This difference is ascribed to the interplay of different effects, such as the device electrostatics, charge transport, defects' occupation, and temperature variation during the breakdown process, which are accounted in GINESTRA while are not included in the simpler thermochemical model of (3).

Inspecting the evolution of the devices during the breakdown process, the most noticeable effect is the alteration of the device electrostatics due to the generation of the positively charged defects. This produces an uneven electric field across the device, with a noticeably higher field near cathode which facilitates further defect formation, leading to positive feedback.

Finally, the bimodal trend exhibited by the thicker devices (i.e., 10 and 22.5 nm) at positive voltage stresses is reproduced allowing for a larger spread ( $\pm 0.1 \text{ eV}$ ) in the activation energy  $E_A$  in the region near the bottom electrode.

As previously stated, the amorphous structure of the considered alumina can explain some degree of variation in Al–O bonds, and thus the activation energy  $E_A$ . The intrinsic defectivity of the oxide could also have a role in the modulation of  $E_A$ , as a highly defective region is expected to have a

different statistics of molecular bonds' distortion with respect to a lesser defective region. Such interpretation is supported by the experimental results, suggesting an asymmetry in both the defect distribution, as discussed in Section III, and in  $E_A$ . This is, however, not a conclusive result and is worth of further investigation.

The values reported in Table II, obtained considering all the discussed effects, are thus a better estimate of the defect generation parameter in a-Al<sub>2</sub>O<sub>3</sub>. This highlights the importance of using a multiscale, atomistic simulation framework to fully understand the microscopic dynamics of the degradation phenomena.

## V. CONCLUSION

In this article, we presented a comprehensive electrical characterization of the atomic defects present in a-Al<sub>2</sub>O<sub>3</sub>. The defects have been profiled by performing an  $I$ – $V$ – $CV$ – $GV$  defect spectroscopy in thin samples (5 nm), and fitting the  $I$ – $V$  curves exhibiting a low-field hysteresis in medium (10 nm) and thick (22.5 nm) samples. The two techniques provide consistent results, identifying defects with  $E_{\text{TH}} = 1.55\text{--}3.55 \text{ eV}$ , in agreement with the *ab initio* calculations on oxygen vacancies and aluminum interstitials reported in literature. The asymmetry of the experimental electrical curves is explained by an asymmetric defect distribution in the devices. The VDDB statistics obtained from RVS measurements have been used for extracting the key parameters of the defect generation process. Atomistic multiscale simulations, performed considering the extracted defect properties, allowed extracting  $E_A \approx 2.4 \text{ eV}$ , in contrast to the results provided by the thermochemical model. The discrepancy is ascribed to the interplay of the device electrostatics, charge transport, charge occupancy, and temperature variation during the breakdown, not accounted in the latter. Furthermore, polarity asymmetries and bimodal trends exhibited by the VDDB statistics are explained by small variations in  $E_A$ , which is expected in amorphous materials such as a-Al<sub>2</sub>O<sub>3</sub>.

## ACKNOWLEDGMENT

All the materials' deposition and device processing, and room temperature electrical measurements, were performed at the CNR-IMM-Unit of Agrate Brianza facilities. The authors acknowledge Mario Alia (CNR-IMM, Agrate Brianza, Italy) for the support in MIM capacitors' fabrication, including metal deposition and lithographic patterning. Moreover, they also thank Isabella Rossetto of STMicelectronics (Agrate Brianza, Italy) for help in  $I$ – $V$  measurements at high temperature for the 5-nm a-Al<sub>2</sub>O<sub>3</sub> capacitors.

## REFERENCES

- [1] K. Yim *et al.*, "Novel high- $k$  dielectrics for next-generation electronic devices screened by automated *ab initio* calculations," *NPG Asia Mater.*, vol. 7, no. 6, p. e190, Jun. 2015, doi: [10.1038/am.2015.57](https://doi.org/10.1038/am.2015.57).
- [2] B. Wang, W. Huang, L. Chi, M. Al-Hashimi, T. J. Marks, and A. Facchetti, "High- $k$  gate dielectrics for emerging flexible and stretchable electronics," *Chem. Rev.*, vol. 118, no. 11, pp. 5690–5754, Jun. 2018, doi: [10.1021/acs.chemrev.8b00045](https://doi.org/10.1021/acs.chemrev.8b00045).
- [3] J. Robertson and R. M. Wallace, "High- $k$  materials and metal gates for CMOS applications," *Mater. Sci. Eng. R Rep.*, vol. 88, pp. 1–41, Feb. 2015, doi: [10.1016/j.mser.2014.11.001](https://doi.org/10.1016/j.mser.2014.11.001).

- [4] Y. Ando, S. Kaneki, and T. Hashizume, "Improved operation stability of Al<sub>2</sub>O<sub>3</sub>/AlGaN/GaN MOS high-electron-mobility transistors grown on GaN substrates," *Appl. Phys. Exp.*, vol. 12, no. 2, Feb. 2019, Art. no. 024002, doi: [10.7567/1882-0786/aafded](https://doi.org/10.7567/1882-0786/aafded).
- [5] S. Y. Lee *et al.*, "Investigation of ultrathin Pt/ZrO<sub>2</sub>-Al<sub>2</sub>O<sub>3</sub>-ZrO<sub>2</sub>/TiN DRAM capacitors Schottky barrier height by internal photoemission spectroscopy," *Current Appl. Phys.*, vol. 17, no. 2, pp. 267–271, Feb. 2017, doi: [10.1016/j.cap.2016.12.004](https://doi.org/10.1016/j.cap.2016.12.004).
- [6] S. Y. Ko *et al.*, "MIM capacitors using ALD Al<sub>2</sub>O<sub>3</sub> for RF IC and DRAM applications," *MRS Online Proc. Library*, vol. 833, pp. 9–13, 2004, doi: [10.1557/PROC-833-G3.10](https://doi.org/10.1557/PROC-833-G3.10).
- [7] Park, S. Heo, J. Chung, and G.-S. Park, "Electron energy loss spectroscopy characterization of TANOS (TaN/Al<sub>2</sub>O<sub>3</sub>/Si<sub>3</sub>N<sub>4</sub>/SiO<sub>2</sub>/Si) Stacks," *Microsc. Microanal.*, vol. 19, pp. 109–113, Aug. 2013, doi: [10.1017/S1431927613012440](https://doi.org/10.1017/S1431927613012440).
- [8] J.-H. Ryu and S. Kim, "Improved intrinsic nonlinear characteristics of Ta<sub>2</sub>O<sub>5</sub>/Al<sub>2</sub>O<sub>3</sub>-based resistive random-access memory for high-density memory applications," *Materials*, vol. 13, no. 18, p. 4201, Sep. 2020, doi: [10.3390/MA13184201](https://doi.org/10.3390/MA13184201).
- [9] H. Duan, W. Fang, L. Liu, and W. Chen, "Theoretical study of bilayer composite barrier based ferroelectric tunnel junction memory," in *Proc. IEEE MTT-S Int. Conf. Numer. Electromagn. Multiphys. Model. Optim. (NEMO)*, Dec. 2020, pp. 1–3, doi: [10.1109/NEMO49486.2020.9343600](https://doi.org/10.1109/NEMO49486.2020.9343600).
- [10] J. Hur, Y. C. Luo, P. Wang, N. Tasneem, A. I. Khan, and S. Yu, "Ferroelectric tunnel junction optimization by plasma-enhanced atomic layer deposition," in *Proc. IEEE Silicon Nanolectron. Workshop (SNW)*, Jun. 2020, pp. 11–12, doi: [10.1109/SNW50361.2020.9131649](https://doi.org/10.1109/SNW50361.2020.9131649).
- [11] R. Goul *et al.*, "Electron tunneling properties of Al<sub>2</sub>O<sub>3</sub> tunnel barrier made using atomic layer deposition in multilayer devices," *AIP Adv.*, vol. 9, no. 2, Feb. 2019, Art. no. 025018, doi: [10.1063/1.5052163](https://doi.org/10.1063/1.5052163).
- [12] X. Liu and J. Shi, "Magnetic tunnel junctions with Al<sub>2</sub>O<sub>3</sub> tunnel barriers prepared by atomic layer deposition," *Appl. Phys. Lett.*, vol. 102, no. 20, May 2013, Art. no. 202401, doi: [10.1063/1.4807132](https://doi.org/10.1063/1.4807132).
- [13] L. Zeng, D. T. Tran, C.-W. Tai, G. Svensson, and E. Olsson, "Atomic structure and oxygen deficiency of the ultrathin aluminium oxide barrier in Al/AlOx/Al Josephson junctions," *Sci. Rep.*, vol. 6, no. 1, pp. 1–8, Sep. 2016, doi: [10.1038/srep29679](https://doi.org/10.1038/srep29679).
- [14] R. Lu *et al.*, "Fabrication of Nb/Al<sub>2</sub>O<sub>3</sub>/Nb Josephson junctions using *in situ* magnetron sputtering and atomic layer deposition," *IEEE Trans. Appl. Supercond.*, vol. 23, no. 3, Jun. 2013, Art. no. 1100705, doi: [10.1109/TASC.2012.2236591](https://doi.org/10.1109/TASC.2012.2236591).
- [15] S. K. Vishwanath, H. Woo, and S. Jeon, "Enhancement of resistive switching properties in Al<sub>2</sub>O<sub>3</sub> bilayer-based atomic switches: Multilevel resistive switching," *Nanotechnology*, vol. 29, Apr. 2018, Art. no. 235202, doi: [10.1088/1361-6528/aa6a3](https://doi.org/10.1088/1361-6528/aa6a3).
- [16] A. Senapati, S. Roy, Y.-F. Lin, M. Dutta, and S. Maikap, "Oxide-electrolyte thickness dependence diode-like threshold switching and high on/off ratio characteristics by using Al<sub>2</sub>O<sub>3</sub> based CBRAM," *Electronics*, vol. 9, no. 7, p. 1106, Jul. 2020, doi: [10.3390/electronics9071106](https://doi.org/10.3390/electronics9071106).
- [17] G. Dingemans and W. M. M. Kessels, "Status and prospects of Al<sub>2</sub>O<sub>3</sub>-based surface passivation schemes for silicon solar cells," *J. Vac. Sci. Technol. A, Vac. Surf. Films*, vol. 30, no. 4, Jul. 2012, Art. no. 040802, doi: [10.1116/1.4728205](https://doi.org/10.1116/1.4728205).
- [18] G. Seguin, E. Cianci, C. Wiemer, D. Saynova, J. A. M. van Roosmalen, and M. Perego, "Si surface passivation by Al<sub>2</sub>O<sub>3</sub> thin films deposited using a low thermal budget atomic layer deposition process," *Appl. Phys. Lett.*, vol. 102, Apr. 2013, Art. no. 131603, doi: [10.1063/1.4800541](https://doi.org/10.1063/1.4800541).
- [19] A. Cappella *et al.*, "High temperature thermal conductivity of amorphous Al<sub>2</sub>O<sub>3</sub> thin films grown by low temperature ALD," *Adv. Eng. Mater.*, vol. 15, no. 11, pp. 1046–1050, Nov. 2013, doi: [10.1002/adem.201300132](https://doi.org/10.1002/adem.201300132).
- [20] S. W. Fong *et al.*, "Thermal conductivity measurement of amorphous dielectric multilayers for phase-change memory power reduction," *J. Appl. Phys.*, vol. 120, no. 1, Jul. 2016, Art. no. 015103, doi: [10.1063/1.4955165](https://doi.org/10.1063/1.4955165).
- [21] O. A. Dicks and A. L. Shluger, "Theoretical modeling of charge trapping in crystalline and amorphous Al<sub>2</sub>O<sub>3</sub>," *J. Phys., Condens. Matter*, vol. 29, no. 31, Aug. 2017, Art. no. 314005, doi: [10.1088/1361-648X/aa7767](https://doi.org/10.1088/1361-648X/aa7767).
- [22] L. S. Salomone, F. Campabadal, and A. Faigón, "Electron trapping in amorphous Al<sub>2</sub>O<sub>3</sub>," *J. Appl. Phys.*, vol. 123, no. 8, Feb. 2018, Art. no. 085304, doi: [10.1063/1.5005546](https://doi.org/10.1063/1.5005546).
- [23] H. Momida and T. Ohno, "Bistability and metastability of oxygen vacancies in amorphous Al<sub>2</sub>O<sub>3</sub>: A possible origin of resistance switching mechanism," *Appl. Phys. Lett.*, vol. 117, no. 10, Sep. 2020, Art. no. 103504, doi: [10.1063/5.0021627](https://doi.org/10.1063/5.0021627).
- [24] B. Kaczer *et al.*, "Considerations for further scaling of metal–insulator–metal DRAM capacitors," *J. Vac. Sci. Technol. B, Nanotechnol. Microelectron. Mater. Process. Meas. Phenomena*, vol. 31, no. 1, Jan. 2013, Art. no. 01A105, doi: [10.1116/1.4767125](https://doi.org/10.1116/1.4767125).
- [25] A. Padovani *et al.*, "A sensitivity map-based approach to profile defects in MIM capacitors from *I*–*V*, *C*–*V*, and *G*–*V* measurements," *IEEE Trans. Electron Devices*, vol. 66, no. 13, pp. 1892–1898, Apr. 2019, doi: [10.1109/TED.2019.2900030](https://doi.org/10.1109/TED.2019.2900030).
- [26] J. Wilt *et al.*, "Atomically thin Al<sub>2</sub>O<sub>3</sub> films for tunnel junctions," *Phys. Rev. Appl.*, vol. 7, no. 6, Jun. 2017, doi: [10.1103/PhysRevApplied.7.064022](https://doi.org/10.1103/PhysRevApplied.7.064022).
- [27] V. V. Afanas'ev, A. Stesmans, B. J. Mrstik, and C. Zhao, "Impact of annealing-induced compaction on electronic properties of atomic-layer-deposited Al<sub>2</sub>O<sub>3</sub>," *Appl. Phys. Lett.*, vol. 81, no. 9, pp. 1678–1680, Aug. 2002, doi: [10.1063/1.1501163](https://doi.org/10.1063/1.1501163).
- [28] S. Jakshik, U. Schroeder, T. Hecht, M. Gutsche, H. Seidl, and J. W. Bartha, "Crystallization behavior of thin ALD-Al<sub>2</sub>O<sub>3</sub> films," *Thin Solid Films*, vol. 425, pp. 216–220, Feb. 2003, doi: [10.1016/S0040-6090\(02\)01262-2](https://doi.org/10.1016/S0040-6090(02)01262-2).
- [29] M. D. Groner, J. W. Elam, F. H. Fabreguette, and S. M. George, "Electrical characterization of thin Al<sub>2</sub>O<sub>3</sub> films grown by atomic layer deposition on silicon and various metal substrates," *Thin Solid Films*, vol. 413, pp. 186–197, Jun. 2002, doi: [10.1016/S0040-6090\(02\)00438-8](https://doi.org/10.1016/S0040-6090(02)00438-8).
- [30] *Applied Materials GinestraTM*. Accessed: Mar. 16, 2022. [Online]. Available: <http://www.appliedmaterials.com/products/applied-mdlx-ginestra-simulation-software>
- [31] L. Larcher, "Statistical simulation of leakage currents in MOS and flash memory devices with a new multiphonon trap-assisted tunneling model," *IEEE Trans. Electron Devices*, vol. 50, no. 5, pp. 1246–1253, May 2003, doi: [10.1109/TED.2003.813236](https://doi.org/10.1109/TED.2003.813236).
- [32] A. Padovani *et al.*, "Statistical modeling of leakage currents through SiO<sub>2</sub>/high-*k* dielectrics stacks for non-volatile memory applications," in *Proc. IEEE Int. Rel. Phys. Symp.*, Apr. 2008, pp. 616–620, doi: [10.1109/RELPHY.2008.455855](https://doi.org/10.1109/RELPHY.2008.455855).
- [33] L. Vandelli, A. Padovani, L. Larcher, R. G. Southwick, W. B. Knowlton, and G. Bersuker, "A physical model of the temperature dependence of the current through SiO<sub>2</sub>/HfO<sub>2</sub> stacks," *IEEE Trans. Electron Devices*, vol. 58, no. 9, pp. 2878–2887, Jul. 2011, doi: [10.1109/TED.2011.2158825](https://doi.org/10.1109/TED.2011.2158825).
- [34] R. Y. Khosa *et al.*, "Electrical characterization of amorphous Al<sub>2</sub>O<sub>3</sub> dielectric films on n-type 4H-SiC," *AIP Adv.*, vol. 8, no. 2, Feb. 2018, Art. no. 025304, doi: [10.1063/1.5021411](https://doi.org/10.1063/1.5021411).
- [35] M. Tian, H. Zhong, L. Li, and Z. Wang, "Polarity dependence degradation mechanism of Al<sub>2</sub>O<sub>3</sub> based metal-insulator-metal antifuse," *J. Appl. Phys.*, vol. 124, no. 24, Dec. 2018, Art. no. 244104, doi: [10.1063/1.5048486](https://doi.org/10.1063/1.5048486).
- [36] R. Y. Khosa *et al.*, "Electrical characterization of amorphous Al<sub>2</sub>O<sub>3</sub> dielectric films on n-type 4H-SiC," *AIP Adv.*, vol. 8, no. 2, Feb. 2018, Art. no. 025304, doi: [10.1063/1.5021411](https://doi.org/10.1063/1.5021411).
- [37] D. Bisi *et al.*, "On trapping mechanisms at oxide-traps in Al<sub>2</sub>O<sub>3</sub>/GaN metal-oxide-semiconductor capacitors," *Appl. Phys. Lett.*, vol. 108, no. 11, Mar. 2016, Art. no. 112104, doi: [10.1063/1.4944466](https://doi.org/10.1063/1.4944466).
- [38] P. L. Torracca, F. Caruso, A. Padovani, S. Spiga, G. Tallarida, and L. Larcher, "Extraction of defects properties in dielectric materials from *I*–*V* curve hysteresis," *IEEE Electron Device Lett.*, vol. 42, no. 2, pp. 220–223, Feb. 2021, doi: [10.1109/LED.2020.3048079](https://doi.org/10.1109/LED.2020.3048079).
- [39] L. Larcher, G. Sereni, and L. Vandelli, "(Invited) defect spectroscopy and engineering for nanoscale electron device applications: A novel simulation-based methodology," *ECS Trans.*, vol. 72, no. 2, pp. 167–177, Apr. 2016, doi: [10.1149/0720.0167ecst](https://doi.org/10.1149/0720.0167ecst).
- [40] L. Larcher, G. Sereni, A. Padovani, and L. Vandelli, "Electrical defect spectroscopy and reliability prediction through a novel simulation-based methodology," in *Proc. Int. Symp. VLSI Technol., Syst. Appl. (VLSI-TSA)*, Apr. 2016, pp. 1–2, doi: [10.1109/VLSI-TSA.2016.7480529](https://doi.org/10.1109/VLSI-TSA.2016.7480529).
- [41] L. Larcher, A. Padovani, D. Pramanik, B. Kaczer, and F. Palumbo, "Defect spectroscopy from electrical measurements: A simulation based technique," in *Proc. IEEE 2nd Electron Devices Technol. Manuf. Conf. (EDTM)*, Mar. 2018, pp. 145–147, doi: [10.1109/EDTM.2018.8421450](https://doi.org/10.1109/EDTM.2018.8421450).
- [42] A. Padovani, L. Larcher, O. Pirrotta, L. Vandelli, and G. Bersuker, "Microscopic modeling of HfO<sub>x</sub> RRAM operations: From forming to switching," *IEEE Trans. Electron Devices*, vol. 62, no. 6, pp. 1998–2006, Jun. 2015, doi: [10.1109/TED.2015.2418114](https://doi.org/10.1109/TED.2015.2418114).

- [43] L. Larcher, A. Padovani, F. M. Puglisi, and P. Pavan, "Extracting atomic defect properties from leakage current temperature dependence," *IEEE Trans. Electron Devices*, vol. 65, no. 12, pp. 5475–5480, Dec. 2018, doi: [10.1109/TED.2018.2874513](https://doi.org/10.1109/TED.2018.2874513).
- [44] D. R. Islamov, V. A. Gritsenko, T. V. Perevalov, O. M. Orlov, and G. Y. Krasnikov, "Mechanism of charge transport of stress induced leakage current and trap nature in thermal oxide on silicon," *J. Phys., Conf. Ser.*, vol. 864, no. 1, pp. 1–5, 2017, doi: [10.1088/1742-6596/864/1/012003](https://doi.org/10.1088/1742-6596/864/1/012003).
- [45] O. A. Dicks, "Computational modelling of defects and charge trapping in amorphous and crystalline metal oxides," Ph.D. dissertation, Dept. Chem., Univ. College London, London, U.K., 2018. [Online]. Available: <https://discovery.ucl.ac.uk/id/eprint/10044113/>
- [46] O. A. Dicks, J. Cottom, A. L. Shluger, and V. V. Afanas'ev, "The origin of negative charging in amorphous Al<sub>2</sub>O<sub>3</sub> films: The role of native defects," *Nanotechnology*, vol. 30, no. 20, May 2019, Art. no. 205201, doi: [10.1088/1361-6528/ab0450](https://doi.org/10.1088/1361-6528/ab0450).
- [47] Z. Guo, F. Ambrosio, and A. Pasquarello, "Oxygen defects in amorphous Al<sub>2</sub>O<sub>3</sub>: A hybrid functional study," *Appl. Phys. Lett.*, vol. 109, no. 6, Aug. 2016, Art. no. 062903, doi: [10.1063/1.4961125](https://doi.org/10.1063/1.4961125).
- [48] D. J. Dumin and J. R. Maddux, "Correlation of stress-induced leakage current in thin oxides with trap generation inside the oxides," *IEEE Trans. Electron Devices*, vol. 40, no. 5, pp. 986–993, May 1993, doi: [10.1109/16.210209](https://doi.org/10.1109/16.210209).
- [49] Z. Xu *et al.*, "A study of relaxation current in high- $k$  dielectric stacks," *IEEE Trans. Electron Devices*, vol. 51, no. 20, pp. 402–408, May 2004, doi: [10.1109/TED.2003.822343](https://doi.org/10.1109/TED.2003.822343).
- [50] D. M. Fleetwood, "'Border traps' in MOS devices," *IEEE Trans. Nucl. Sci.*, vol. 39, no. 2, pp. 269–271, Apr. 1992, doi: [10.1109/23.277495](https://doi.org/10.1109/23.277495).
- [51] T. L. Thompson and J. T. Yates, "TiO<sub>2</sub>-based photocatalysis: Surface defects, oxygen and charge transfer," *Topics Catalysis*, vol. 35, nos. 3–4, pp. 197–210, Jul. 2005, doi: [10.1007/s11244-005-3825-1](https://doi.org/10.1007/s11244-005-3825-1).
- [52] Q. Yang, K. Kalathiparambil, D. T. Elg, D. Ruzic, and W. M. Kriven, "Microstructural damage of  $\alpha$ -Al<sub>2</sub>O<sub>3</sub> by high energy density plasma," *Acta Mater.*, vol. 132, pp. 479–490, Jun. 2017, doi: [10.1016/j.actamat.2017.04.058](https://doi.org/10.1016/j.actamat.2017.04.058).
- [53] E. O. Filatova, A. S. Konashuk, F. Schaefers, and V. V. Afanas'ev, "Metallization-induced oxygen deficiency of  $\gamma$ -Al<sub>2</sub>O<sub>3</sub> layers," *J. Phys. Chem. C*, vol. 120, no. 16, pp. 8979–8985, Apr. 2016, doi: [10.1021/acs.jpcc.6b01352](https://doi.org/10.1021/acs.jpcc.6b01352).
- [54] A. Berman, "Time-zero dielectric reliability test by a ramp method," in *Proc. 19th Int. Rel. Phys. Symp.*, Apr. 1981, pp. 204–209, doi: [10.1109/IRPS.1981.362997](https://doi.org/10.1109/IRPS.1981.362997).
- [55] G. S. Haase and J. W. McPherson, "Modeling of interconnect dielectric lifetime under stress conditions and new extrapolation methodologies for time-dependent dielectric breakdown," in *Proc. 45th Annu. IEEE Int. Rel. Phys. Symp.*, Apr. 2007, pp. 390–398, doi: [10.1109/RELPHY.2007.369921](https://doi.org/10.1109/RELPHY.2007.369921).
- [56] J. McPherson, J.-Y. Kim, A. Shanware, and H. Mogul, "Thermochemical description of dielectric breakdown in high dielectric constant materials," *Appl. Phys. Lett.*, vol. 82, no. 13, pp. 2121–2123, Mar. 2003, doi: [10.1063/1.1565180](https://doi.org/10.1063/1.1565180).
- [57] J. W. McPherson, J. Kim, A. Shanware, H. Mogul, and J. Rodriguez, "Trends in the ultimate breakdown strength of high dielectric-constant materials," *IEEE Trans. Electron Devices*, vol. 50, no. 8, pp. 1771–1778, Aug. 2003, doi: [10.1109/TED.2003.815141](https://doi.org/10.1109/TED.2003.815141).
- [58] E. Y. Wu, "Facts and myths of dielectric breakdown processes—Part I: Statistics, experimental, and physical acceleration models," *IEEE Trans. Electron Devices*, vol. 66, no. 11, pp. 4523–4534, Nov. 2019, doi: [10.1109/TED.2019.2933612](https://doi.org/10.1109/TED.2019.2933612).
- [59] F. Campabadal *et al.*, "Electrical characteristics of metal-insulator-semiconductor structures with atomic layer deposited Al<sub>2</sub>O<sub>3</sub>, HfO<sub>2</sub>, and nanolaminates on different silicon substrates," *J. Vac. Sci. Technol. B, Nanotechnol. Microelectron. Mater. Process. Meas. Phenomena*, vol. 29, no. 1, Jan. 2011, Art. no. 01AA07, doi: [10.1116/1.3532544](https://doi.org/10.1116/1.3532544).
- [60] A. Padovani, L. Larcher, G. Bersuker, and P. Pavan, "Charge transport and degradation in HfO<sub>2</sub> and HfO<sub>x</sub> dielectrics," *IEEE Electron Device Lett.*, vol. 34, no. 5, pp. 680–682, May 2013, doi: [10.1109/LED.2013.2251602](https://doi.org/10.1109/LED.2013.2251602).
- [61] P. La Torraca, F. M. Puglisi, A. Padovani, and L. Larcher, "Multiscale modeling for application-oriented optimization of resistive random-access memory," *Materials*, vol. 12, no. 21, p. 3461, Oct. 2019, doi: [10.3390/ma12213461](https://doi.org/10.3390/ma12213461).
- [62] A. Padovani and L. Larcher, "Time-dependent dielectric breakdown statistics in SiO<sub>2</sub> and HfO<sub>2</sub> dielectrics: Insights from a multiscale modeling approach," in *Proc. IEEE Int. Rel. Phys. Symp. (IRPS)*, Mar. 2018, pp. 3A.2-1–3A.2-7, doi: [10.1109/IRPS.2018.8353552](https://doi.org/10.1109/IRPS.2018.8353552).
- [63] J. H. Lim *et al.*, "Investigating the statistical-physical nature of MgO dielectric breakdown in STT-MRAM at different operating conditions," in *IEDM Tech. Dig.*, Dec. 2018, pp. 25.3.1–25.3.4, doi: [10.1109/IEDM.2018.8614515](https://doi.org/10.1109/IEDM.2018.8614515).
- [64] A. Ranjan *et al.*, "Boron vacancies causing breakdown in 2D layered hexagonal boron nitride dielectrics," *IEEE Electron Device Lett.*, vol. 40, no. 8, pp. 1321–1324, Aug. 2019, doi: [10.1109/LED.2019.2923420](https://doi.org/10.1109/LED.2019.2923420).